


Using First-Principles Calculations in CALPHAD Models to Determine Carrier Concentration of the Binary PbSe Semiconductor

MATTHEW C. PETERS ,^{1,3} JEFF W. DOAK,² J.E. SAAL,² G.B. OLSON,^{1,2} and P.W. VOORHEES¹

1.—Department of Materials Science and Engineering, Northwestern University, Evanston, IL, USA. 2.—QuesTek Innovations LLC, Evanston, IL, USA. 3.—e-mail: matthewpeters2013@u.northwestern.edu

PbSe is a promising thermoelectric that can be further improved by nanostructuring, band engineering, and carrier concentration tuning; therefore, a firm understanding of the defects in PbSe is necessary. The formation energies of point defects in PbSe are computed via first-principles calculations under the dilute-limit approximation. We find that under Pb-rich conditions, PbSe is an *n*-type semiconductor dominated by doubly-charged Se vacancies. Conversely, under Se-rich conditions, PbSe is a *p*-type semiconductor dominated by doubly-charged Pb vacancies. Both of these results agree with previously performed experiments. Temperature- and chemical potential-dependent Fermi levels and carrier concentrations are found by enforcing the condition of charge neutrality across all charged atomic and electronic states in the system. The first-principles-predicted charge-carrier concentration is in qualitative agreement with experiment, but slightly varies in the magnitude of carriers. To better describe the experimental data, a CALPHAD assessment of PbSe is performed. Parameters determined via first-principles calculations are used as inputs to a five-sublattice CALPHAD model that was developed explicitly for binary semiconductors. This five sublattice model is in contrast to previous work which treated PbSe as a stoichiometric compound. The current treatment allows for experimental carrier concentrations to be accurately described within the CALPHAD formalism. In addition to the five-sublattice model, a two-sublattice model is also developed for use in multicomponent databases. Both models show excellent agreement with the experimental data and close agreement with first-principles calculations. These CALPHAD models can be used to determine processing parameters that will result in an optimized carrier concentration and peak zT value.

Key words: Thermoelectrics, CALPHAD, first-principles, DFT, defect chemistry

INTRODUCTION

The application of thermoelectric materials in waste-heat recovery has been limited due to their low efficiency.¹ The figure of merit, zT , of a

thermoelectric is a measure of its efficiency and is given by the formula $ZT = S^2\sigma T/\kappa$, where S , σ , T , and κ are the Seebeck coefficient, electrical conductivity, temperature, and thermal conductivity, respectively. Lead-based chalcogenides are some of the highest performing thermoelectric materials for mid to high temperature applications of 500–900 K.² In particular, PbTe, PbS, and PbSe have been the focus of recent research.^{3–8} The zT of these

(Received May 25, 2018; accepted November 16, 2018; published online December 3, 2018)

compounds can be increased through several processes that emphasize different contributions to zT .^{3,9} Introducing nano-scale precipitates, which scatter heat-carrying phonons without adversely affecting the electrical conductivity, can reduce the thermal conductivity.⁴ In addition, the electrical transport properties can be enhanced through band engineering.^{9,10}

PbSe is a promising thermoelectric material as it is able to take advantage of all of the previous methods in its own system as well as enhancing the thermoelectric properties of other systems discussed below. The carrier concentration of PbSe can be tuned via Na doping,¹¹ which can be further improved by band engineering through alloying with Sr.¹² PbSe contains two valence bands, L and Σ , which dominate carrier transport at low and high temperatures, respectively.¹² Electronic transport properties are optimized at temperatures where these bands contribute relatively equally to carrier transport (so called band convergence). In pristine PbSe, the temperature at which band convergence occurs is above 900 K, which limits the use of pristine PbSe for thermoelectric applications. However, introducing Sr to PbSe decreases the band-convergence temperature into a more applicable range, resulting in a net increase of zT . It should be noted that recent research has cast doubt on this simplified model between the L and Σ bands, suggesting instead that the two bands become interconnected for highly doped materials.¹³ However, it is clear that band engineering plays a critical role in optimizing the electronic transport properties.^{10,12,14} PbSe has also been shown to improve the thermoelectric performance in PbTe. The PbTe-PbSe system exhibits a solid solution for many temperatures and compositions.¹⁵ Therefore, the addition of PbSe to PbTe provides point defects that scatter short-wavelength phonons. Similar to PbSe, PbTe also contains the two valence bands, L and Σ , however its convergence temperature is much lower, around 450 K.¹⁰ The electronic transport properties can be enhanced if this convergence temperature occurs at a higher temperature, which can be achieved by alloying with PbSe, which as noted previously, has a convergence temperature closer to 900 K. Therefore, alloying PbTe with PbSe not only increases the overall power factor of the material, but also lowers the thermal conductivity by introducing point defects that scatter heat-carrying phonons.¹⁰

In order to fully optimize the zT of these materials, a precise understanding of the system's phase diagram is required. Knowledge of the phase diagram can be used to determine the composition and processing parameters necessary to achieve the optimal microstructure for enhanced zT of the thermoelectric system. In addition, the carrier concentration can be used to determine the Seebeck coefficient and electrical conductivity, which can be determined by the solubility of intrinsic defects and

ternary elements in PbSe. First-principles calculations can provide important insights into the dominant defects in the PbSe system.¹⁶ The CALculation of PHase Diagram (CALPHAD) method is also a proven approach to model experimental data and create phase diagrams.¹⁷ Often, the models used in CALPHAD depend on parameters that are difficult or impossible to determine via experiments. The coupling of first-principles calculations and experimental data in CALPHAD assessments has been shown to yield physically sound models.¹⁸

Numerous studies have investigated the PbSe system through first-principles calculations and experimental thermodynamic modeling. Lin, Sharma, and Chang (LSC)¹⁹ and Liu et al.²⁰ both provide an extensive review of the thermodynamic information of the Pb-Se system. In the LSC study, a thermodynamic model first developed for SnTe²¹ is used to describe the off-stoichiometric nature of PbSe. While a satisfactory agreement between experiments and model is achieved in the LCS study, a number of improvements can be made. The model employed in the LCS study has not seen widespread use, and; therefore, incorporation within a multicomponent database would be impractical and also requires more fitting variables (five) than the models presented here. In addition, the assessment was done by fitting to solubility lines on the phase diagram, which are determined from carrier concentration experiments. This procedure overweighs data at higher temperatures, where the carrier concentration and deviation from stoichiometry is higher due to the linear relationship between carriers and off-stoichiometry. Lastly, the conversion of carrier concentration to solubility limits appears to be inconsistent with previous studies.^{22,23} The thermodynamic model performed by Liu et al. uses the well-established compound energy formalism (CEF), however, they treat PbSe as a line compound, and; therefore, all information on the carriers of the systems is lost. PbSe has also previously been studied using first-principles calculations. Li et al. determined defect formation energies for a range of defects in the PbX (X = S, Se, Te) system, however, their study was limited to neutral defects, which can exhibit much higher formation energies than charged defects.²⁴ A study by Wrass, Venezuela and Baierle investigated defects in bulk and nanowire PbSe and PbTe.²⁵ Although their study includes charged defects as well as spin-orbit (SO) interactions, their study did not investigate the solvus boundaries of the system. Their defect formation energies span a range of Fermi levels and provide no insight on the magnitude of defects within the system. Bajaj et al. recently used the dilute-limit approximation to calculate the solvus boundaries in Na-doped PbSe, however, they do not report the defects of the binary system.²⁶

The goal of this work is to model the carrier concentration of the PbSe compound. Charge carriers in semiconducting systems are created by

defects as well as thermal excitation; therefore, information on the dominant defects of the system is necessary to ensure a physically accurate model. To achieve this, first-principles calculations using density functional theory (DFT) have been performed on neutral and charged defects. Formation energies are then determined by enforcing charge neutrality under the dilute limit, which determines the Fermi level of the system under a specific growth condition. Using this technique, the formation energy, concentration of defects and carriers of the system can be determined. The information derived from first-principles calculations such as the dominant defects, formation energy, and ionization energy, will be used in developing thermodynamic models based on the CEF, which can be easily implemented in multicomponent databases and commercially available software to be used in material design.

The first-principles calculations indicate that doubly ionized vacancies on the Pb and Se site are the dominant defects in Se-rich and Pb-rich growth conditions. The predicted carrier concentration agrees qualitatively with the experimental data but differs in overall magnitude. To achieve a better description of the experimental data, two CEF models have been investigated. A five-sublattice (5SL) model developed explicitly for binary semiconductors and a multicomponent two-sublattice (2SL) model have been developed that show excellent agreement with each other as well as the experimental data. These models add to the growing subject of how best to address defects within CALPHAD models.^{27–31} Both of these models use fitting parameters that are linked to values derived from the first-principles calculations to give them greater physical significance. This work is another example^{18,30–34} of how first-principles calculations and the CALPHAD method are able to complement one another and also addresses how to develop multicomponent compatible models that involve vacancies.

Numerous studies have investigated the PbSe system through first-principles calculations and experimental thermodynamic modeling, but none have combined the two to provide an accurate description of the intrinsic carriers.^{19,20,25} This study focuses on determining the dominant defects and their associated formation energies using density functional theory (DFT) and the dilute-limit approximation. These parameters will be used as inputs into a five-sublattice CALPHAD model that has been previously developed explicitly for binary semiconductors to describe the carrier concentration and solubility limits of PbSe. A recent CALPHAD assessment of the Pb-Se system treated PbSe as a stoichiometric phase,²⁰ thereby losing all information of the intrinsic carriers. It is also important to note that the published solubility limits in Liu et al.'s study appear to be inconsistent.¹⁹

COMPUTATIONAL METHODOLOGY

Defect Formation Energies

In order to determine the dominant defects of the system, the formation energy of defects in the system must be known. First-principles calculations have been successfully used in similar systems and that approach has been used here.^{16,35} The dilute-limit approximation is used to determine the formation energy and concentration of the defects in the PbSe system. The formation energy of a defect is calculated as³⁶

$$\begin{aligned} \Delta E_f^j(\Delta\mu, \Delta\mu_e) = & [E^j - E^0] - \sum_{i=1}^N \Delta N_i^j (\mu_i^0 + \Delta\mu_i) \\ & - \Delta N_e^j (E_{\text{VBM}} + \Delta V_{\text{PA}} + \Delta\mu_e) + \Delta E_{\text{IC}}, \end{aligned} \quad (1)$$

where E^0 and E^j are the total energies of the defect-free and defect containing supercell for defect j , respectively. ΔN_i^j is the number of atoms of type i removed ($\Delta N_i^j < 0$) or added ($\Delta N_i^j > 0$) from the system. μ_i^0 is the chemical potential of atom i in its standard reference state (fcc for Pb and hexagonal for Se) and $\Delta\mu_i$ is the change in chemical potential of element i relative to its standard reference state dependent on the equilibrium conditions, i.e., Pb-rich or Se-rich. Similar to ΔN_i^j , ΔN_e^j is the number of electrons added or removed from the system, where ΔN_e^j is greater than zero for electrons added to the system and less than zero for electrons removed from the system. E_{VBM} is the energy of the valence band, ΔV_{PA} a potential alignment term, and $\Delta\mu_e$ the Fermi level of the system relative to the E_{VBM} . Lastly, ΔE_{IC} is an image charge correction term. The parameters E^0 , E^j , μ_i^0 , $\Delta\mu_i$, and E_{VBM} can all be derived from the DFT calculations, ΔV_{PA} and ΔE_{IC} are post-processing correction terms, and $\Delta\mu_e$ can numerically be solved for as described below.

The chemical potentials of Pb and Se are given by their DFT determined total energies in their stable structure at 298 K and 1 atmospheric pressure, known as their stable-element reference (SER) state. The chemical potential, μ_i , is unchanged when in equilibrium with the SER of an atom. Therefore, under Pb-rich conditions, the chemical potential of Pb is equal to μ_i^0 and is equal to zero. Since there are no other stable phases in equilibrium with PbSe other than the SER of Pb and Se, the chemical potential of Se is then fixed by the chemical potential of PbSe, μ_{PbSe} , which is calculated from the chemical potential of its constituents, μ_{Pb} and μ_{Se} ³⁷:

$$\mu_{\text{Pb}} + \mu_{\text{Se}} = \mu_{\text{PbSe}}. \quad (2)$$

Under Pb-rich conditions the chemical potential of μ_{Se} is reduced from its SER. The same process can

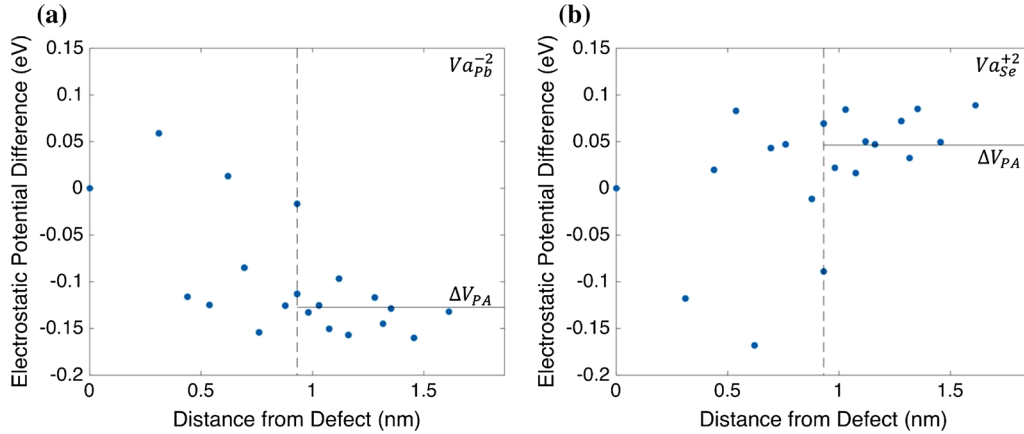


Fig. 1. The potential alignment term for defects, (a) Va_{Pb}^{-2} and (b) Va_{Se}^{+2} . The potential alignment is determined by averaging the difference in electrostatic potential from the defect and defect-free supercell for atoms equal to one half of the periodic image distance.

be used to determine the change in chemical potential of a Pb atom in a Se-rich environment in equilibrium with hexagonal Se. Since these are the only two solid phases in equilibrium with PbSe, no further adjustment of chemical potentials are necessary.

The creation of charged defects in a supercell calculation with periodic boundary conditions requires correction terms for which many methods exist to determine them. To ensure charge neutrality conditions are not violated, a background neutralizing charge is introduced, which affects the potential of the calculation.³⁸ The shift in potential means that the energy levels of a defect containing supercell and a defect-free supercell are not directly comparable and thus an adjustment, taking the form of a constant offset, is required. In addition, periodic boundary conditions mean that charged defects interact with each other, and therefore, do not actually represent isolated defects in the bulk. Lany and Zunger³⁸ (LZ) utilize a simple method where the potentials of the bulk and charged defect super cells are aligned at a distance far from the defect and a Markov-Payne expansion is used to correct for image charge interactions. This correction scheme has been used successfully in a number of similar studies with success,^{16,26,35,39} however, this involves double counting the effect of the image charge interaction as it is not explicitly taken into account when aligning the potentials. Freysoldt et al.⁴⁰ (FNV) developed a method that first models the charge of the defect using a Gaussian or point charge model. The potentials from a neutral and charged defect are then used to correct the shift in potentials. This method corrects the double counting issue that is introduced in the LZ method. Kumagai and Oba⁴¹ built on the FNV method, making it more general and useful in systems that exhibit large atomic relaxations. This study employs the LZ scheme despite the double counting of the image charge contribution as it will be shown that the image charge is quite small, due to the large

dielectric constant, and a recent paper that shows minimal effects for cubic systems.⁴² By assuming that the electrostatic potential far away from the defect should be identical to that of the host cell, the offset can be determined. The offset is determined by calculating the average difference in electrostatic potential around each atom in the supercells between the defect cell, $\overline{V_{el,i}^d}$, and the perfect cell, $\overline{V_{el,i}^0}$, at a distance greater than or equal to one half the distance between periodic image defects,

$$\Delta V_{PA} = \frac{1}{N} \sum \left(\overline{V_{el,i}^d} - \overline{V_{el,i}^0} \right). \quad (3)$$

A graphical representation of this is shown in Fig. 1. In this study, the value ΔV_{PA} for various defects ranges from near zero to approximately 0.1 eV in magnitude. The largest offset was found to be -0.13 eV for a negatively charged (-2) vacancy on the Pb site.

In addition to the potential alignment term, we must also correct for the defect-defect interactions that occur due the periodic boundary conditions. The corrections are determined through a Markov-Payne expansion, which is given to third order in L for a 3-D array of length, L ⁴³

$$\Delta E_{IC} = \frac{q^2 \alpha}{2L\eta} + \frac{2\pi q Q}{3L^3 \eta} + O(L^{-5}), \quad (4)$$

where α is the Madelung constant (1.75) of the periodic array of defects, Q the second radial moment of the charge density, and η the dielectric constant. The dielectric constant is calculated to be 232 for PbSe, which agrees with the room temperature value of 204. This large dielectric constant drastically reduces the image correction term such that it has a negligible effect on the formation energies, as has been seen in other studies.^{16,26,35} This also indicates that the image charge plays a small role in the potential alignment term calculated previously.

Computational Approach

The total energies of the perfect and defect containing supercell were determined by DFT^{44,45} calculations performed with the Vienna *Ab initio* Simulation Package⁴⁶ (VASP)⁴⁷ with projector-augmented wave⁴⁸ (PAW) potentials utilizing the generalized gradient functional of Perdew, Burke, and Ernzerhof⁴⁹ (PBE). These calculations treat the $6s^26p^2$ and $4s^24p^4$ electrons as valence in the Pb and Se atoms, respectively. The NaCl crystal structure for PbSe was taken from the Inorganic Crystal Structure Database⁵⁰ (ICSD). For the defect calculations, $3 \times 3 \times 3$ supercells were created from the conventional unit cell of PbSe and contain 216 total atoms. Structures were allowed to relax with a maximum cutoff energy of 350 eV and Monkhorst–Pack $4 \times 4 \times 4$ k-point meshes.⁵¹ These parameters were determined to converge the defect formation energies to within 15 meV with respect to cutoff energies and Monkhorst–Pack k-point meshes. Lattice parameters and atomic positions were allowed to relax until energy convergence reached 0.1 meV and a final static calculation was performed to determine the total energy. The dielectric constant was calculated using density functional perturbation theory implemented in VASP and includes ionic contributions.^{52–54}

Defect Concentration To determine the concentration of defects, the formation energies of the defects and, thus, the Fermi level of the system must be known. To fix the Fermi level, the charge neutrality condition must be enforced

$$\sum_j \Delta N_e^j n_j + n^- - p^+ = 0, \quad (5)$$

where n_j is the number of defects j per formula unit, and n^- and p^+ are the concentration of electrons and holes, respectively. To determine the number density of electrons and holes under the rigid band approximation, the density of states, $g(E)$, determined via first-principles calculations, can be multiplied by the Fermi function and integrated over the appropriate energy levels:

$$n^-(T, \Delta\mu_e) = \int_{E_g}^{\infty} g(E) \frac{1}{1 + e^{(E - \Delta\mu_e)/k_B T}} dE, \quad (6)$$

$$p^+(T, \Delta\mu_e) = \int_{-\infty}^0 g(E) \frac{1}{1 + e^{(\Delta\mu_e - E)/k_B T}} dE. \quad (7)$$

All energies here are relative to the valence band maximum and E_g is the band gap of the host material. The concentration of point defects n_j is given by a simple Arrhenius equation under the dilute-limit approximation³⁶

$$n_j(T, \Delta\mu, \Delta\mu_e) = N_{\text{site}}^j e^{-\Delta E_f^j/k_B T}, \quad (8)$$

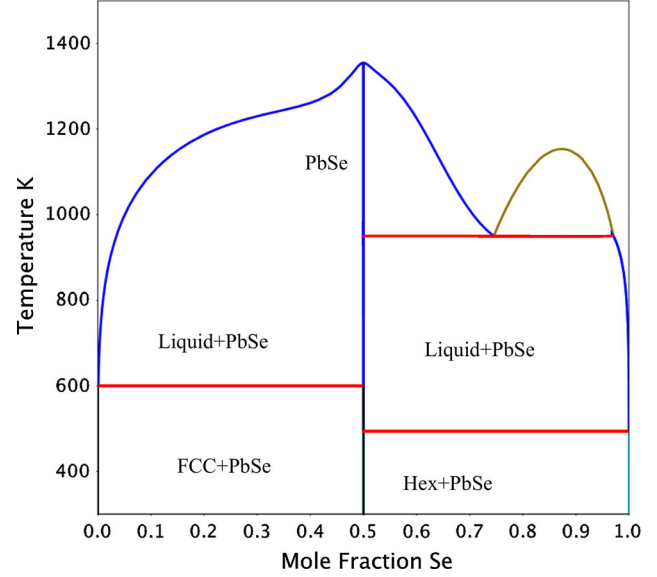


Fig. 2. The parameters from Liu et al.²⁰ were used to calculate the Pb–Se phase diagram here where the PbSe phase is modeled as a stoichiometric compound.

where N_{site}^j is the number of possible sites for defect j in the formula unit and ΔE_f^j is calculated using Eq. 1. Equations 6, 7, and 8 are combined with the charge neutrality condition, Eq. 5, which yields the Fermi level, $\Delta\mu_e$, for a given temperature. This allows for the enthalpy of formation as well as concentration of electrons, holes, and defects to then be determined.

CALPHAD Modeling

Due to the small homogeneity range of PbSe, it has generally been considered a stoichiometric compound. The most recent assessment performed by Liu et al. does exactly this.²⁰ Their assessment has a reasonable description of the liquidus, invariant points, and enthalpy of mixing in the liquid. For this reason, the parameters for the liquid and stoichiometric PbSe have been taken from this study and used here. The calculated phase diagram using their parameters is shown in Fig. 2.

Five-Sublattice Model

The focus of this study is to describe the intrinsic carriers of PbSe. To achieve this, PbSe is modeled using a five-sublattice (5SL) model developed by Chen et al. to describe binary semiconductors.⁵⁵ This model is based on one described by Oates et al. using the species chemical potential/bond energy (SCPBE).⁵⁶ It has been used to describe the GaAs, CdTe, GaN, ZnO, PbTe, and PbS semiconducting systems.^{55,57–59}

The 5SL model for PbSe is described as: $(\mathbf{Pb}, \mathbf{Va}^-)(\mathbf{Se}, \mathbf{Va}, \mathbf{Va}^{+2})(\mathbf{Va})(\mathbf{Va}, \mathbf{e}^{-1})(\mathbf{Va}, \mathbf{h}^{+1})$, where the first, second, third, fourth, and fifth sublattices are

the Pb-site, Se-site, interstitial-site, electron, and hole sublattices. As will be shown later, doubly-charged vacancies are the dominant defects in the system. Interstitial defects have high formation energies and are not considered here, however, the sublattice is left for completeness and possible extrapolation into ternary systems where doping occurs on the interstitial sites. Mathematically, the 5SL model is calculated using the standard procedure for the compound energy formalism (CEF) as

$$G^{\text{PbX}} = \sum_i \sum_j \sum_k \sum_l \sum_m y_i^{\text{Pb}} y_j^{\text{Se}} y_k^{\text{I}} y_l^{\text{e}} y_m^{\text{h}} G_{ijklm} + RT \left(\sum_i y_i^{\text{Pb}} \ln y_i^{\text{Pb}} + \sum_j y_j^{\text{Se}} \ln y_j^{\text{Se}} + \sum_k y_k^{\text{I}} \ln y_k^{\text{I}} + \sum_l y_l^{\text{e}} \ln y_l^{\text{e}} + \sum_m y_m^{\text{h}} \ln y_m^{\text{h}} \right), \quad (9)$$

where y_i^s represents the site fraction of i on sublattice s , R is the gas constant, and T is temperature. G_{ijklm} is the end-member representing a system that is completely filled with components i, j, k, l , and m on the first, second, third, fourth, and fifth sublattice, respectively; modeling of these end-members will be discussed below. Introducing charged species in this model requires an extra constraint when minimizing the Gibbs free energy, as the phase has to be electrically neutral. The total number of end-members in this system is 36, however, first-principles calculations and assumptions allow these end-members to be calculated in a straightforward manner.

The two end-members of greatest importance are those containing electrons and holes. Chen et al. determined that these end-members can be modeled as⁵⁵

$${}^0G_{\text{PbSeVae}^{-1}\text{Va}} + {}^0G_{\text{PbSeVaVah}^{+1}} = 2{}^0G_{\text{PbSeVaVaVa}} + E_g - RT(\ln N_e + \ln N_h), \quad (10)$$

where E_g is the experimental band gap of PbSe, ${}^0G_{\text{PbSeVaVaVa}}$ is the Gibbs free energy of stoichiometric PbSe taken from Liu et al.'s study²⁰ and N_e and N_h are the effective density of states for non-degenerate semiconductors given by:

$$N_{e,h} = 2 \left(\frac{2\pi m_{e,h}^* kT}{h^2} \right)^{3/2} \left(\frac{a^3}{4} \right), \quad (11)$$

where $m_{e,h}^*$, k , h , and a are the effective masses of the electron and holes, Boltzmann constant, Planck's constant, and lattice parameters, respectively. The parameter $\left(\frac{a^3}{4}\right)$ converts the effective density of states into a density per formula unit, thereby making it compatible with the CEF. The parameters for PbSe can be taken from the literature and are summarized in Table II. An appropriate reference state for the Gibbs free energy of electrons and holes is chosen as the middle of the band gap, where the Fermi level is assumed to be for non-degenerate semi-conductors and as previous

authors have chosen.⁵⁹ Following the definition of Eq. 10, the end-members can be defined as:

$${}^0G_{\text{PbSeVae}^{-1}\text{Va}} = {}^0G_{\text{PbSeVaVaVa}} + \frac{E_g}{2} - RT \ln N_e, \quad (12)$$

$${}^0G_{\text{PbSeVaVah}^{+1}} = {}^0G_{\text{PbSeVaVaVa}} + \frac{E_g}{2} - RT \ln N_h. \quad (13)$$

End-members containing charged defects on one of the first two sublattices represent the ionization of their respective neutral defect. The charged defects of interest in the PbSe system are doubly-charged vacancies, therefore, each defect creates two electrons or holes. These end-members are modeled as

$${}^0G_{\text{Va}^{-2}\text{SeVaVaVa}} = {}^0G_{\text{VaSeVaVaVa}} - 2{}^0G_{\text{PbSeVaVah}^{+1}} + 2{}^0G_{\text{PbSeVaVaVa}} + \Delta E_{\text{VaPb}^{-2}}, \quad (14)$$

$${}^0G_{\text{PbVa}^{+2}\text{VaVaVa}} = {}^0G_{\text{PbVaVaVaVa}} - 2{}^0G_{\text{PbSeVae}^{-1}\text{Va}} + 2{}^0G_{\text{PbSeVaVaVa}} + \Delta E_{\text{VaSe}^{+2}}. \quad (15)$$

Here the values $\Delta E_{\text{VaPb}^{-2}}$ and $\Delta E_{\text{VaSe}^{+2}}$ are the ionization energies or defect transition energies of the neutral vacancies on the Pb and Se sublattice, respectively. These are determined by calculating the Fermi level at which the neutral and charged defect are equal to one another. These energies are assumed to be independent of temperature, and; therefore, the values determined by first-principles calculations can be used and are given in Table II.

To determine end-members that contain two defects on the first two sublattices a reciprocal relation is utilized. In order to minimize the chances for the formation of a miscibility gap, the reciprocal energy is assumed to be zero¹⁷ and the end-members are calculated as

$${}^0G_{\text{ijVaVaVa}} = {}^0G_{\text{iSeVaVaVa}} + {}^0G_{\text{PbjVaVaVa}} - {}^0G_{\text{PbSeVaVaVa}}. \quad (16)$$

In addition, any end-member that contains three or more defects is assumed to have a Gibbs free energy equal to zero. This assumption is reasonable due to the small concentration of defects in the system such that the site fraction of any individual defect is near zero. According to Eq. 9, any end-member with three or more defects will be multiplied by a number near zero three or more times. Therefore, any physically reasonable number can be chosen without a large contribution to the Gibbs free energy of the phase and here, zero is chosen for convenience.

This leaves two remaining end-members to be assessed, which represent the single neutral defects of the system:

$${}^0G_{\text{PbVaVaVaVa}} = {}^0G_{\text{Pb}}^{\text{fcc}} + V_1 + V_2 T, \quad (17)$$

$${}^0G_{\text{VaSeVaVaVa}} = {}^0G_{\text{Se}}^{\text{orth}} + V_3 + V_4 T. \quad (18)$$

The parameters V_1 to V_4 are the variables that are allowed to change to fit the experimental data. Specifically, V_1 and V_3 represent the enthalpy of formation of a Se and Pb vacancy on the Se and Pb site, respectively. These values can be determined by first-principles calculations and are used as starting points for our optimizations. The optimization is done through the PARROT⁶⁰ module of ThermoCalc.⁶¹ The parameters ${}^0G_{\text{Pb}}^{\text{fcc}}$ and ${}^0G_{\text{Se}}^{\text{orth}}$ are the Gibbs free energy of Pb and Se in their stable element reference (SER) and are taken from Dinsdale⁶² and are also used for the fcc and orthogonal phase, respectively. The liquid phase description is taken from the recent assessment performed by Liu et al.²⁰ *Two-Sublattice Model*

In addition to the 5SL model, a two-sublattice (2SL) model is developed to describe the PbSe phase. Although the 5SL model can accurately describe the carrier concentration of PbSe and contains many of the physical parameters used in semiconductor physics, it is not compatible in a multicomponent database. The neutral defect containing end-members ${}^0G_{\text{PbVaVaVaVa}}$ and ${}^0G_{\text{VaSeVaVaVa}}$ can be found in other systems such as PbTe and PbS. Therefore, there would be an incompatibility when combining assessments from other binaries. To address this, a 2SL model is developed that is fully compatible with other systems.

It will be shown that vacancies are the predominant defects in this system, and; therefore, the 2SL model can be described as **(Pb,Va)(Se,Va)**. The stoichiometric composition divides the phase diagram, such that on the Pb-rich solidus side, the number of vacancies on the Se sublattice is orders of magnitude larger than on the Pb sublattice. Therefore, when modeling the Pb-rich solidus, the phase can be assumed to be equivalent to Pb(Se,Va) and reduces the degrees of freedom to one, the site fraction of Se or Va on the Se sublattice. The equilibrium site fraction of vacancies can then be determined by minimizing the grand potential

$$\mathcal{G}_m = G_m - \mu_{\text{Pb}}y_{\text{Pb}} - \mu_{\text{Se}}y_{\text{Se}}, \quad (19)$$

where \mathcal{G}_m , μ_{Pb} , and μ_{Se} are the grand potential per mole and chemical potential of Pb and Se atoms, respectively. The molar Gibbs free energy can be calculated by the CEF as

$$G_m = y_{\text{Se}} {}^0G_{\text{PbSe}} + y_{\text{Va}} {}^0G_{\text{PbVa}} + RT(y_{\text{Se}} \ln(y_{\text{Se}}) + y_{\text{Va}} \ln(y_{\text{Va}})) + y_{\text{Se}}y_{\text{Va}}L_{\text{Se,Va}}. \quad (20)$$

Taking the derivative of Eq. 19 with respect to y_{Se} and since μ_{Se} is constant in the two-phase region, setting the result equal to zero leads to the equilibrium y_{Se}

$$0 = \frac{dG_m}{dy_{\text{Se}}} - \mu_{\text{Se}}. \quad (21)$$

Substituting the derivative of Eq. 20 with respect to y_{Se} into Eq. 20 leads to

$$-{}^0G_{\text{PbVa}} + {}^0G_{\text{PbSe}} + L_{\text{Se,Va}}(1 - 2y_{\text{Se}}) - \mu_{\text{Se}} = RT \ln\left(\frac{y_{\text{Se}}}{1 - y_{\text{Se}}}\right). \quad (22)$$

The equilibrium site fraction of vacancies can then be calculated by substituting $1 - y_{\text{Va}}$ for y_{Se} and assuming a dilute concentration, where $y_{\text{Va}} \ll 1$

$$y_{\text{VaSe}}^{\text{eq}} = \exp\left(-\frac{{}^0G_{\text{PbVa}} - {}^0G_{\text{PbSe}} + L_{\text{Se,Va}} + \mu_{\text{Se}}}{RT}\right). \quad (23)$$

The numerator of Eq. 23 is equivalent to the energy of formation for a vacancy per mole formula unit in Pb-rich conditions. This value can be and has been determined via first-principles calculations. The real advantage of the 2SL model is that the energy of formation is split between a structure specific parameter, ${}^0G_{\text{PbVa}}$ and a system specific parameter $L_{\text{Se,Va}}$. Therefore, once a value of ${}^0G_{\text{PbVa}}$ has been chosen, the interaction parameter can be changed to fit the experimental data or first-principles calculations in a given system. The stoichiometric end-member is determined from the previous assessment, and the chemical potential is fixed by the two-phase region representative of the solidus lines. A similar derivation for the Se-rich solidus leads to an equivalent formula,

$$y_{\text{VaPb}}^{\text{eq}} = \exp\left(-\frac{{}^0G_{\text{VaSe}} - {}^0G_{\text{PbSe}} + L_{\text{Pb,Va}} + \mu_{\text{Pb}}}{RT}\right). \quad (24)$$

A reasonable value for the Gibbs free energy must be given to the end-members containing vacancies, and there is much discussion in the CALPHAD community concerning these.^{29,30,63,64} Initially, a value of zero was chosen for vacancies; however, at high temperatures these end-members would become stable and, therefore, are not physically reasonable. For this study a value of $2.3RT$ is used as suggested by Rogal et al.'s recent article,²⁹ which is in agreement with Franke's analysis of a number greater than $\ln(2 - 1/2)RT$ to ensure a unique solution.⁶⁴ A positive penalty function also ensures that the PbSe phase does not become stable at either the Pb or Se end of the phase diagram.

The end-members of the 2SL model are then

$${}^0G_{\text{PbVa}} = {}^0G_{\text{Pb}}^{\text{fcc}} + 2.3RT, \quad (25)$$

$${}^0G_{\text{VaSe}} = {}^0G_{\text{Se}}^{\text{SER}} + 2.3RT, \quad (26)$$

$${}^0G_{\text{VaVa}} = 4.6RT. \quad (27)$$

And the interaction parameters can be linked to the formation energies by

$$L_{\text{Pb,Va}} = G_{\text{VaPb}}^f - {}^\circ G_{\text{VaSe}} + {}^\circ G_{\text{PbSe}} - \mu_{\text{Pb}}, \quad (28)$$

$$L_{\text{Se,Va}} = G_{\text{VaSe}}^f - {}^\circ G_{\text{PbVa}} + {}^\circ G_{\text{PbSe}} - \mu_{\text{Se}}. \quad (29)$$

RESULTS AND DISCUSSION

DFT Calculations

In order to determine the dominant defects in PbSe, both antisite and vacancy defects ranging in charge from -2 to $+2$ are considered. Equations 1, 5, 6, 7, and 8 are used to solve for the Fermi level, from which defect formation energies and concentration of defects as a function of temperature are determined. The range of Fermi levels, calculated by the charge neutrality condition as a function of temperature and equilibrium conditions, is shown in Fig. 3. The Fermi level under Se-rich conditions approaches the valence band maximum, causing p -type carriers in the system. Conversely, under Pb-

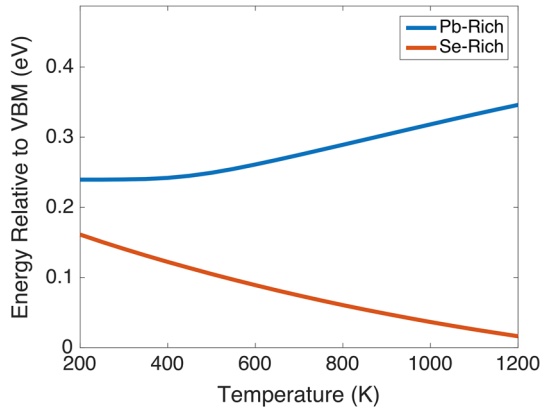


Fig. 3. Calculated Fermi level as a function of temperature. Fermi levels are calculated by enforcing charge neutrality at a given temperature.

rich conditions, the Fermi level lies much closer to the conduction band resulting in n -type carriers. This result matches the qualitative results of the Fermi levels found in experimental investigations.

The formation energies of various defects as functions of the Fermi level are shown in Fig. 4. The temperature-dependent Fermi levels calculated from the charge neutrality condition are also shown. Under Pb-rich conditions, the defect $\text{Va}_{\text{Se}}^{+2}$ is the lowest formation energy for all Fermi energies. Similarly, the $\text{Va}_{\text{Pb}}^{-2}$ defect is lowest in Se-rich conditions. These are consistent with the results found in both the PbS and PbTe systems in similar studies.^{16,25,35} In addition, the doubly ionized vacancies are consistent with experimental evidence for vacancies playing the dominant role as defects within this system. Ohashi ruled out interstitial defects as playing a role and identified vacancies as the dominant defects in their selenium partial pressure effects on carrier concentration investigation.⁶⁵ This result is also in agreement with Chou's study, whose maximum solubility measurements could only be explained if vacancy defects were assumed.⁶⁶

The ionization energy, or transition energy, of the doubly ionized vacancies required for the CALPHAD model can also be calculated from these figures. The ionization energy of a defect is the Fermi level at which the neutral defect and charged defect are the same.⁶⁷ The ionization energy of $\text{Va}_{\text{Pb}}^{-2}$ and $\text{Va}_{\text{Se}}^{+2}$ are -0.13 eV and 0.49 eV relative to the valence band maximum, respectively. Due to the disagreement of the DFT calculated band gap of 0.487 eV and the temperature dependent experimental band gap of 0.275 eV at 300 K,⁶⁸ these transition energies are scaled as a fraction of the DFT derived band gap and converted to an equivalent fraction of the experimental band gap to be used in the 5SL model.³⁵ This is necessary as the CALPHAD model parameters are fit to experimental data and use the experimentally determined

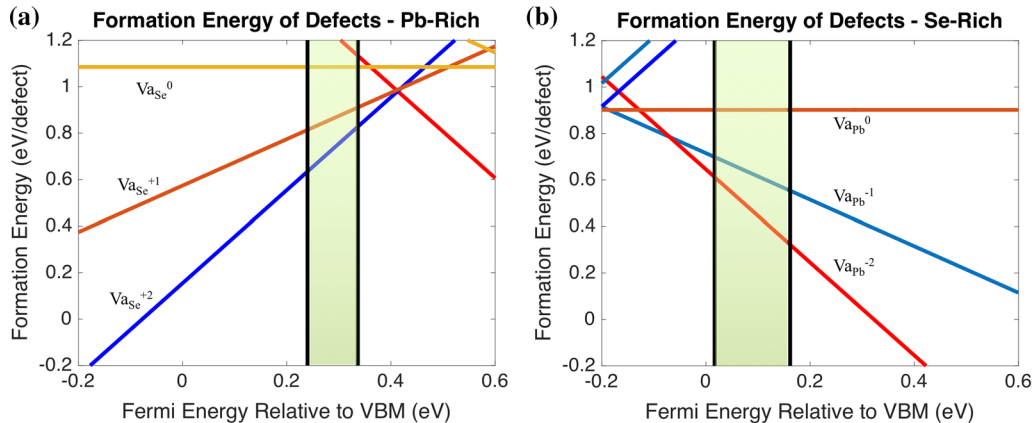


Fig. 4. Formation energies of various defects as predicted by DFT as a function of the Fermi energy relative to the valence band edge (VBM) for (a) Pb-rich conditions and (b) Se-rich conditions. By enforcing charge neutrality, a range of possible Fermi levels can be determined as shown in the shaded region. Doubly-ionized vacancies have the lowest formation energy in either condition.

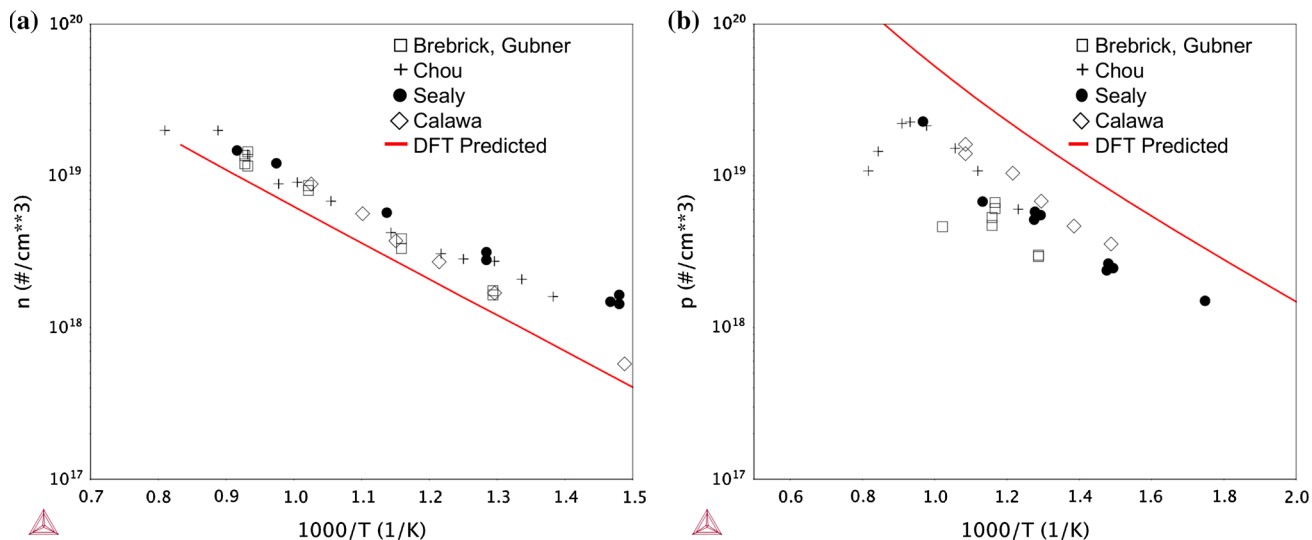


Fig. 5. DFT predicted carrier concentrations with experimental data for (a) Pb-rich conditions and (b) Se-rich conditions. The calculations agree qualitatively, however, disagree on the magnitude. This could be due to the difference in equilibrium conditions, as much of the experimental data is in equilibrium with the liquid, or the error in the predicted band gap.

band gap to describe the electron and hole energies. Use of the DFT determined energies without scaling, would be inconsistent with the rest of the model and used in previous models.^{35,69} These values are given in Table II.

The DFT predicted carrier concentrations are shown in Fig. 5 along with experimental data from several studies.^{66,70–72} The calculations are in qualitative agreement with the experimental data. However, the DFT calculations under predict the experimental carrier concentration in the Pb-rich condition and over predict it in the Se-rich regime. The slope, with respect to inverse temperature, agrees well with experiment, however, the magnitude of carriers is in slight disagreement for Pb-rich and even more so in Se-rich conditions. This discrepancy is likely due to the difference in equilibrium conditions in the experiment, where PbSe is in equilibrium with liquid or solid Pb and Se. Conversely, the calculations only take into account being in equilibrium with solid Pb or Se. In addition, the disagreement between the calculated and room temperature band gap could also play a role. Calculations that include spin-orbit coupling (SOC) could provide greater accuracy as they more accurately predict the band gap of these materials, but are much more computationally expensive.⁷³ Lastly, vibrational formation entropy is not considered here, which has been shown to improve the accuracy of first-principles calculations.^{31,74} Nonetheless, the agreement between the slope of the calculations and experimental data should provide confidence that our enthalpies of formation, as given in Table I for various defects, are accurate.

Based on these results, the CALPHAD model will consist of doubly ionized vacancies on the Pb and Se lattice, along with their associated neutral defects

Table I. Formation values as calculated by DFT in Pb-rich and Se-rich growth conditions

PbSe formation energies at 300 K as determined by DFT (eV/defect)

Defect	Pb-rich conditions	Se-rich conditions
Va_{Se}^{+2}	0.59	1.60
Va_{Se}^{+1}	0.82	1.90
Va_{Se}^0	1.08	2.25
Va_{Pb}^{-2}	1.33	0.32
Va_{Pb}^{-1}	2.59	0.55
Va_{Pb}^0	2.06	0.90
Va_{Pb}^{+1}	2.59	1.35

that will serve as optimizing parameters. The formation energies of neutral vacancies has also been calculated, which are not affected by the error in band gap measurements as their formation energies are independent of the Fermi level according to Eq. 1. The 5SL model uses non-degenerate semiconductor physics to describe the Gibbs free energy of electrons and holes of the ionized system. These parameters are well documented in the literature and are summarized in Table II. The neutral defects serve as reference values for the end-members containing ionized defects and the DFT energies are used as a starting point for the optimization, listed in Table III. The 2SL model does not contain the semiconductor physics, however, as shown in “Two-Sublattice Model” section, parameters of the model can be linked to the

formation energy of the charged defects, which are compared in Table IV.

CALPHAD Modeling

The inaccuracies of the DFT calculations can be addressed through CALPHAD modeling. However, the assessment of this system would be extremely difficult if not for the insight provided by the first-principles calculations discussed above. The formation energies of the neutral vacancies are used as starting parameters for V_1 and V_3 and are allowed to vary, along with a temperature dependent term to describe the experimental data. The final optimized parameters are given in Table III along with the associated first-principles calculation.

The optimized CALPHAD parameters agree qualitatively with the DFT calculations in that the formation energy of a Se vacancy is smaller than that of a Pb vacancy. In addition, the errors of the final parameters do not vary by more than 15% from the DFT predicted values. The carrier concentrations under Pb-rich and Se-rich conditions are shown in Fig. 6. The CALPHAD method matches experiment and DFT by describing hole and electron generation in the Se-rich and Pb-rich regime, respectively. The CALPHAD model also does an excellent job of describing the carrier concentration through the entire temperature range and shows great improvement from the DFT calculations alone, see Fig. 5.

By assuming that a single type of defect dominates the carriers, the carrier concentration can be converted to solubility limits using the equation²²:

$$X_m = 0.5 + \frac{(p-n)M_{\text{PbSe}}}{4Z\rho N_A}, \quad (30)$$

where M_{PbSe} is the molar mass of PbSe, Z the ionization of the defect, ρ the density, and N_A Avogadro's number. The phase diagram of PbSe is plotted in Fig. 7 along with the converted experimental data points. The CALPHAD model does an excellent job of describing this data, particularly at lower temperatures. The model begins to deviate slightly at higher temperatures, which is due to the exponential growth of carriers and the linear relationship it has with solubility. No CEF model with solubility has been assessed; as such we are unable to compare it to past work. As mentioned previously, the assessment seen in Lin¹⁹ differs by a factor of two due to an inconsistency when converting the carrier concentration to solidus data. An assessment has also been done where the solubility limits were used as experimental data in lieu of carrier concentration. This led to a better description of the high temperature phase diagram; however, the carrier concentrations at low temperatures are poorly described. In addition, the optimized end-member converged farther from the starting DFT values when fitting to the solubility limits. For these reasons, coupled with the fact that the carrier concentration is the important data for semiconductors, this procedure is not recommended here.

The 2SL model is shown as magenta in Figs. 6 and 7, and the 2SL model shows an agreement with experiment very similar to that of the 5SL model. The only large deviations occur at higher temperatures in the phase diagram where the discrepancy in carrier concentration is magnified. This is because the solubility limit is linearly proportional to the carrier concentration. Therefore, small deviations at high temperature where the carrier concentration is large will be much larger in the phase diagram. The final optimized parameters are given in Table IV along with the formation energies determined by the CALPHAD method and DFT. The CALPHAD values agree qualitatively with the first-principles calculations in that the formation of a Pb vacancy is smaller in magnitude than a Se vacancy. They are also in close quantitative agreement, differing by no more than 16% in magnitude. This 2SL model is also fully compatible with other binaries, as the end-members have not been fit to the experimental data. Although the 2SL model is much simpler and does not contain many of the

Table II. Parameters used in the 5SL CALPHAD model and references. Ionization energies were calculated from first-principles calculations and scaled to the experimental band gap at 300 K

PbSe parameters for CALPHAD model	
Eg (eV)	0.329 ^a
a (nm)	0.612 ^a
m_e^*/m_0	0.27 ^b
m_h^*/m_0	0.27 ^b
$\Delta E_{V_{\text{a-Pb}}^{-2}}$ (J/mol)	-7000
$\Delta E_{V_{\text{a-Se}}^{+2}}$ (J/mol)	55.0

^aRef. 68. ^bRef. 75.

Table III. Optimized parameters for 5SL CALPHAD model. The first-principles calculations for the formation of a neutral vacancy are also provided and used as starting points for the optimization

End-member	Optimized parameter (J/mol)	First-principles calculation (J/mol)
${}^0G_{\text{PbVaVaVaVa}}$	${}^0G_{\text{Pb}}^{\text{fcc}} + 118,661 + 68.7T$	105,000
${}^0G_{\text{VaSeVaVaVa}}$	${}^0G_{\text{Se}}^{\text{Hex}} + 98,482 + 84.3T$	87,000

Table IV. Interaction parameters for the PbSe 2SL model

Interaction parameter	Optimized value (J/mol)	CALPHAD determined formation energy at 300 K (J/mol)	DFT predicted formation energy at 300 K (J/mol)
$L_{\text{Pb,Va:Se}}$	37,954	42,000	31,000
$L_{\text{Pb:Se,Va}}$	45,585	51,000	57,000

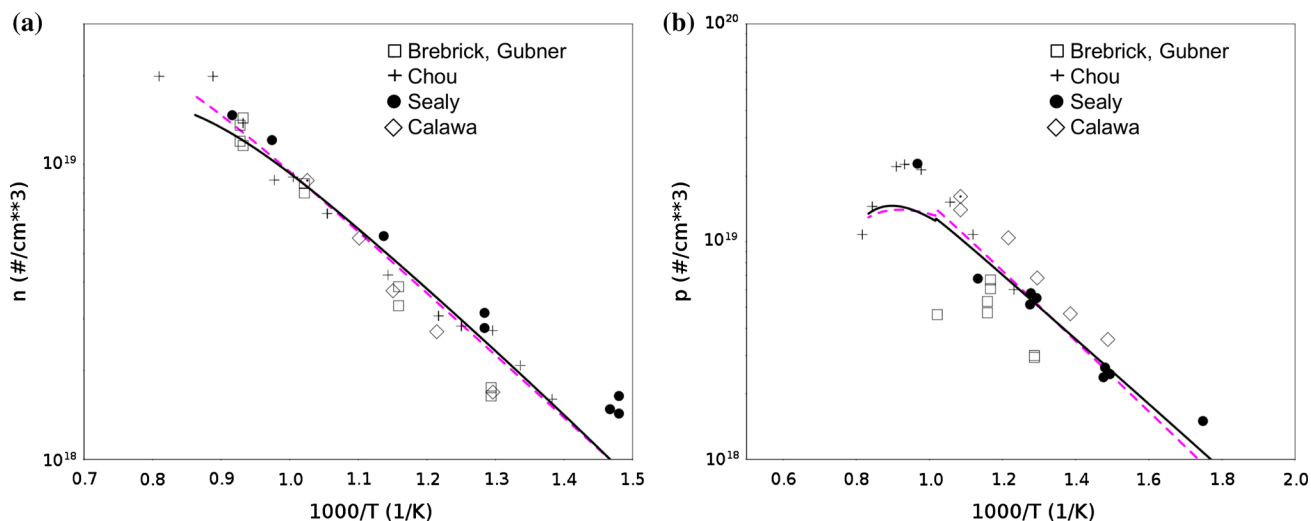


Fig. 6. Carrier concentration as described by the 5SL CALPHAD model shown in solid black for (a) Pb-rich conditions and (b) Se-rich conditions. The experimental data is well described by the 5SL model and shows large improvement from the DFT predicted values. The 2SL model is shown in dashed magenta and describes the data equally well.

CONCLUSIONS

First-principles calculations of PbSe have been performed to determine the dominant defects under the dilute-limit approximation. DFT results show that doubly-ionized vacancies on the Pb and Se site under Se-rich and Pb-rich conditions respectively, have the lowest formation energy for a large range of Fermi levels. The charge neutrality condition was used to determine possible ranges of the Fermi level, formation energies, and concentration of carriers for PbSe. The DFT predicted carrier concentrations are in qualitative agreement with the experimental data, however, the predicted carrier concentrations disagree slightly on the overall magnitude of carriers as determined by experiment.

To better describe the carriers of the system, a 5SL CALPHAD model developed explicitly for semiconductors was used to assess the system. The CALPHAD model used the dominant defects as determined by DFT as well as their transition energies and neutral defect formation energies as parameters within the model. The CALPHAD assessment shows a much better agreement to the experimental data and describes both the carrier concentration as well as the solubility of PbSe reasonably well. A simplified 2SL model has also been developed that can be used in multicomponent databases. It shows similar agreement to the experimental data and is also in close agreement with the

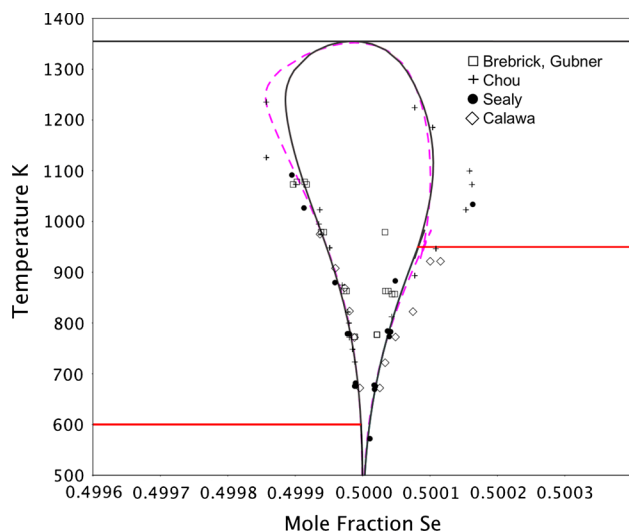


Fig. 7. Enlarged phase region of PbSe where the carrier concentration has been converted to solubility points assuming doubly ionized vacancies. The 2SL model is shown in dashed magenta and closely follows the 5SL model shown in solid black.

physical parameters that are found in the 5SL model, its close agreement between the 5SL model, experimental data, and first-principles calculations indicate that it is physically sound.

first-principles calculations for the formation energy of charged defects as well as that of the 5SL model indicating that its parameters are physically consistent. This study is yet another example of the benefit that CALPHAD has when working with first-principles calculations. In addition, this CALPHAD assessment provides greater physical accuracy than previous CALPHAD descriptions and can be used when assessing multicomponent Pb-chalcogenide systems.

ACKNOWLEDGMENTS

The authors gratefully acknowledge thermoelectrics research at Northwestern University through the Center for Hierarchical Materials Design (CHiMaD) and financial support from the DARPA SIMPLEX program through SPAWAR (Contract #N66001-15-C-4036). M. Peters was supported by the Department of Defense (DoD) through the National Defense Science & Engineering Graduate Fellowship (NDSEG) Program.

FUNDING

Funding was provided by Defense Advanced Research Projects Agency and National Institute of Standards and Technology (US).

REFERENCES

1. F.J. DiSalvo, *Science* 285, 703 (1999).
2. G.J. Tan, L.D. Zhao, and M.G. Kanatzidis, *Chem. Rev.* 116, 12123 (2016).
3. K. Biswas, J.Q. He, I.D. Blum, C.I. Wu, T.P. Hogan, D.N. Seidman, V.P. Dravid, and M.G. Kanatzidis, *Nature* 489, 414 (2012).
4. G.J. Tan, F.Y. Shi, S.Q. Hao, L.D. Zhao, H. Chi, X.M. Zhang, C. Uher, C. Wolverton, and V.P. Dravid, *Nat. Commun.* 7, 12167 (2016).
5. J.P. Heremans, C.M. Thrush, and D.T. Morelli, *Phys. Rev. B* 70, 5 (2004).
6. J. Androulakis, C.H. Lin, H.J. Kong, C. Uher, C.I. Wu, T. Hogan, B.A. Cook, T. Caillat, K.M. Paraskevopoulos, and M.G. Kanatzidis, *J. Am. Chem. Soc.* 129, 9780 (2007).
7. Y.Z. Pei, Z.M. Gibbs, A. Gloskovskii, B. Balke, W.G. Zeier, and G.J. Snyder, *Adv. Energy Mater.* 4, 12 (2014).
8. Y.Z. Pei, A.D. LaLonde, N.A. Heinz, and G.J. Snyder, *Adv. Energy Mater.* 2, 670 (2012).
9. L.D. Zhao, H.J. Wu, S.Q. Hao, C.I. Wu, X.Y. Zhou, K. Biswas, J.Q. He, T.P. Hogan, C. Uher, C. Wolverton, V.P. Dravid, and M.G. Kanatzidis, *Energy Environ. Sci.* 6, 3346 (2013).
10. Y.Z. Pei, A. LaLonde, S. Iwanaga, and G.J. Snyder, *Energy Environ. Sci.* 4, 2085 (2011).
11. H. Wang, Y.Z. Pei, A.D. LaLonde, and G.J. Snyder, *Adv. Mater.* 23, 1366 (2011).
12. H. Wang, Z.M. Gibbs, Y. Takagiwa, and G.J. Snyder, *Energy Environ. Sci.* 7, 804 (2014).
13. C.M. Jaworski, M.D. Nielsen, H. Wang, S.N. Girard, W. Cai, W.D. Porter, M.G. Kanatzidis, and J.P. Heremans, *Phys. Rev. B* 87, (4) (2013).
14. Q. Zhang, F. Cao, W.S. Liu, K. Lukas, B. Yu, S. Chen, C. Opeil, D. Broido, G. Chen, and Z.F. Ren, *J. Am. Chem. Soc.* 134, 10031 (2012).
15. J. Steininger, *Metall. Trans.* 1, 2939+ (1970).
16. J.W. Doak, K.J. Michel, and C. Wolverton, *J. Mater. Chem. C* 3, 10630 (2015).
17. H.L. Lukas, *Computational Thermodynamics The Calphad Method* (Cambridge: Cambridge University Press, 2007).
18. Z.K. Liu, *J. Phase Equilib. Diffus.* 30, 517 (2009).
19. J.C. Lin, R.C. Sharma, and Y.A. Chang, *J. Phase Equilib.* 17, 253 (1996).
20. Y. Liu, Z. Kang, G. Sheng, L. Zhang, J. Wang, and Z. Long, *J. Electron. Mater.* 41, 1915 (2012).
21. J.C. Lin, T.L. Ngai, and Y.A. Chang, *Metall. Trans. A* 17, 1241 (1986).
22. J.C. Lin, K.C. Hsleh, R.C. Sharma, and Y.A. Chang, *Bull. Alloy Phase Diagr.* 10, 340 (1989).
23. J.C. Lin, R.C. Sharma, and Y.A. Chang, *Bull. Alloy Phase Diagr.* 7, 374 (1986).
24. W.F. Li, C.M. Fang, M. Dijkstra, and M.A. van Huis, *J. Phys.: Condens. Matter* 27, 14 (2015).
25. E.O. Wrasse, P. Venezuela, and R.J. Baierle, *J. Appl. Phys.* 116, 183703 (2014).
26. S. Bajaj, H. Wang, J.W. Doak, C. Wolverton, and G.J. Snyder, *J. Mater. Chem. C* 4, 1769 (2016).
27. A.N. Grundy, E. Povoden, T. Ivas, and L.J. Gauckler, *CALPHAD* 30, 33 (2006).
28. A. Saengdeejing, J.E. Saal, V.R. Manga, and Z.K. Liu, *Acta Mater.* 60, 7207 (2012).
29. J. Rogal, S.V. Divinski, M.W. Finnis, A. Glensk, J. Neugebauer, J.H. Perepezko, S. Schuwalow, M.H.F. Sluiter, and B. Sundman, *Phys. Status Solidi B* 251, 97 (2014).
30. P.W. Guan and Z.K. Liu, *Scr. Mater.* 133, 5 (2017).
31. P.W. Guan, S.L. Shang, G. Lindwall, T. Anderson, and Z.K. Liu, *CALPHAD* 59, 171 (2017).
32. K. Ozturk, Y. Zhong, L.Q. Chen, C. Wolverton, J.O. Sofo, and Z.K. Liu, *Metall. Mater. Trans. A* 36A, 5 (2005).
33. L.J. Zhang, J. Wang, Y. Du, R.X. Hu, P. Nash, X.G. Lu, and C. Jiang, *Acta Mater.* 57, 5324 (2009).
34. Y. Zhong, C. Wolverton, Y.A. Chang, and Z.K. Liu, *Acta Mater.* 52, 2739 (2004).
35. S. Bajaj, G.S. Pomrehn, J.W. Doak, W. Gierlotka, H.J. Wu, S.W. Chen, C. Wolverton, W.A. Goddard, and G.J. Snyder, *Acta Mater.* 92, 72 (2015).
36. C.G. Van de Walle and J. Neugebauer, *J. Appl. Phys.* 95, 3851 (2004).
37. C. Freysoldt, B. Grabowski, T. Hickel, J. Neugebauer, G. Kresse, A. Janotti, and C.G. Van de Walle, *Rev. Mod. Phys.* 86, 253 (2014).
38. S. Lany and A. Zunger, *Phys. Rev. B* 78, 235104 (2008).
39. A. Goyal, P. Gorai, E.S. Toberer, and V. Stevanovic, *Npj Comput. Mater.* 3, Article number 42 (2017).
40. C. Freysoldt, J. Neugebauer, and C.G. Van de Walle, *Phys. Rev. Lett.* 102, (1) (2009).
41. Y. Kumagai and F. Oba, *Phys. Rev. B* 89, 195205 (2014).
42. T.R. Durrant, S.T. Murphy, M.B. Watkins, and A.L. Shluger, *J. Chem. Phys.* 149, (2) (2018).
43. G. Makov and M.C. Payne, *Phys. Rev. B* 51, 4014 (1995).
44. W. Kohn and L.J. Sham, *Phys. Rev.* 140, 1133 (1965).
45. P. Hohenberg and W. Kohn, *Phys. Rev. B* 136, B864 (1964).
46. G. Kresse and J. Hafner, *Phys. Rev. B* 49, 14251 (1994).
47. G. Kresse and J. Furthmuller, *Phys. Rev. B* 54, 11169 (1996).
48. G. Kresse and D. Joubert, *Phys. Rev. B* 59, 1758 (1999).
49. J.P. Perdew, K. Burke, and M. Ernzerhof, *Phys. Rev. Lett.* 77, 3865 (1996).
50. A. Belsky, M. Hellenbrandt, V.L. Karen, and P. Luksch, *Acta Crystallogr. Sect. B Struct. Sci.* 58, 364 (2002).
51. H.J. Monkhorst and J.D. Pack, *Phys. Rev. B* 13, 5188 (1976).
52. M. Gajdos, K. Hummer, G. Kresse, J. Furthmuller, and F. Bechstedt, *Phys. Rev. B* 73, 045112 (2006).
53. S. Baroni and R. Resta, *Phys. Rev. B* 33, 7017 (1986).
54. X. Wu, D. Vanderbilt, and D.R. Hamann, *Phys. Rev. B* 72, 035105 (2005).
55. Q. Chen, M. Hillert, B. Sundman, W.A. Oates, S.G. Fries, and R. Schmid-Fetzer, *J. Electron. Mater.* 27, 961 (1998).
56. W.A. Oates, G. Eriksson, and H. Wenzl, *J. Alloys Compd.* 220, 48 (1995).
57. Q. Chen and M. Hillert, *J. Alloys Compd.* 245, 125 (1996).
58. J.B. Li and J.C. Tedenac, *J. Electron. Mater.* 31, 321 (2002).
59. J.B. Li and L.L. Kerr, *Opt. Mater.* 35, 1213 (2013).

60. B. Jansson, Ph.D. thesis, Royal Institute of Technology, Stockholm, Sweden (1984).
61. B. Sundman, B. Jansson, and J.O. Andersson, *CALPHAD* 9, 153 (1985).
62. A.T. Dinsdale, *CALPHAD* 15, 317 (1991).
63. A.T. Dinsdale, A.V. Khvan, and A. Watson, *Mater. Sci. Technol.* 30, 1715 (2014).
64. P. Franke, *J. Phase Equilib. Diffus.* 35, 780 (2014).
65. N. Ohashi and K. Igaki, *Trans. Jpn. Inst. Met.* 5, 94 (1964).
66. N. Chou, K. Komarek, and E. Miller, *Trans. Metall. Soc. AIME* 245, 1553 (1969).
67. A.F. Kohan, G. Ceder, D. Morgan, and C.G. Van de Walle, *Phys. Rev. B* 61, 15019 (2000).
68. O. Madelung, *Semiconductors: Data Handbook*, 3rd ed. (Berlin: Springer, 2004).
69. M.C. Peters, J.W. Doak, W.-W. Zhang, J.E. Saal, G.B. Olson, and P.W. Voorhees, *CALPHAD* 58, 17 (2017).
70. A.R. Calawa, T.C. Harman, M. Finn, and P. Youtz, *Trans. Metall. Soc. AIME* 242, 374 (1968).
71. B.J. Sealy and A.J. Crocker, *J. Mater. Sci.* 8, 1737 (1973).
72. R.F. Brebrick and E. Gubner, *J. Chem. Phys.* 36, 170 (1962).
73. N. Wang, D. West, J.W. Liu, J. Li, Q.M. Yan, B.L. Gu, S.B. Zhang, and W.H. Duan, *Phys. Rev. B* 89, 045142 (2014).
74. J.W. Doak, C. Wolverton, and V. Ozolins, *Phys. Rev. B* 92, 174306 (2015).
75. H. Wang, Y.Z. Pei, A.D. LaLonde, and G.J. Snyder, *Proc. Natl. Acad. Sci. U.S.A.* 109, 9705 (2012).